# Active hyperspectral imager using a tunable supercontinuum light source based on a MEMS Fabry–Perot interferometer

Kääriäinen, Teemu; Dönsberg, Timo

*Published in:*
Optics Letters

*DOI:*
10.1364/OL.439551

Published: 15/11/2021

*Document Version*
Publisher's final version

Optics Letters

# Active hyperspectral imager using a tunable supercontinuum light source based on a MEMS Fabry–Perot interferometer

Teemu Kääriäinen* and Timo Dönsberg

*VTT Technical Research Centre of Finland, Tekniikantie 1, 02150, Espoo, Finland*
**Corresponding author: teemu.kaariainen@vtt.fi*

*Received 4 August 2021; revised 7 October 2021; accepted 9 October 2021; posted 19 October 2021 (Doc. ID 439551); published 3 November 2021*

**We have developed an active hyperspectral imager based on a tunable near-infrared supercontinuum light source. Non-dispersive wavelength selection of the supercontinuum laser source is achieved with a microelectromechanical Fabry–Perot interferometer. The tunable light source enables the use of any monochromatic imaging sensor with a suitable spectral sensitivity for hyperspectral imaging. The imager is characterized and demonstrated in the laboratory for remote detection of ice.** 

https://doi.org/10.1364/OL.439551

Hyperspectral (HS) imaging refers to a method where each pixel of an image is measured with a broad continuum of wavelengths. The spectral information contained within each pixel can be used to extract non-visual information of the target. HS imaging is used, for example, in medical imaging [1], food inspection and quality control [2], and mineral survey [3]. Most commercial HS cameras are designed as so-called push broom imagers, where a single spatial line is measured at a given moment. The line imaging HS camera uses a spectrograph to disperse different wavelengths to the second dimension of the detector matrix. These systems are ideal for imaging conveyor belts or aerial applications, where the targets move past the imaged line. For two-dimensional (2D) imaging of stationary targets, mechanical scanning is required. This can be achieved, for example, with a moving platform for the sample under the HS camera, or by rotating or translating the camera. For 2D imaging without mechanical scanning, HS cameras with interferometric filtering can be used. Scanning Fabry–Perot interferometer (FPI) filters offer a convenient solution for spectral filtering in 2D HS imagers [4,5]. Another non-mechanical scanning approach for HS imaging is single-pixel imaging, which is typically done using digital micromirror devices [6–8].

Each spectral channel in a HS image consists of light from only a narrow wavelength region. Therefore, lighting requirements are demanding, regardless of the HS imaging technology used. Especially in the infrared (IR) part of the optical spectrum, light is usually not abundant in any indoor space, due to non-thermal illumination sources. Outdoor imaging, on the other hand, is restricted to clear sunny days. Artificial broadband light sources in the IR range are typically thermal. This is a clear limitation for field and drone operation of HS cameras, due to the high power consumption and size of the thermal light sources required to provide sufficient illumination. Moreover, HS imaging typically requires a spectral reference target in the vicinity of the imaged target to account for the spectral and intensity fluctuations of the thermal illumination source, which can be highly unpractical. Applications such as airplane, runway, or highway icing detection, mineral mapping in an active mine, rescue operations at night, or HS imaging for mobile robotics require operation regardless of illumination conditions and without a constant spectral reference at the target area. Currently, none of the existing HS imagers meets these demands.

Supercontinuum (SC) generation refers to the spectral broadening of monochromatic light in a nonlinear medium, such as an optical fiber [9]. High brightness combined with a broad spectrum and high spatial coherence make SC a promising illumination source for HS sensors and imagers. SC can be generated for IR wavelengths, where suitable thermal generation is highly inefficient and high-power LED sources are not widely available. Moderate power SC (<1 W) can be readily generated in a compact form factor using commercial pump lasers. High-power SC sources, providing up to hundreds of watts of optical power, have also been demonstrated [10,11]. So far, the published work on SC based HS sensing and imaging has mostly been single point and scanning single point systems [12–18]. These approaches can allow long detection distances [13], because the whole SC output power is concentrated on a single pixel, in contrast to imaging devices, where the illumination is spread over the imaging region. For some applications, the operation distance can be compromised for a faster acquisition rate of an imaging device. To this day, the combination of SC light sources and HS imaging devices remains relatively unexplored [19,20].

In this work, we demonstrate a novel approach of an active HS imager (AHI) using a SC light source and a tunable microelectromechanical (MEMS) Fabry–Perot interferometer (FPI) developed at the Technical Research Centre of Finland (VTT) [21–23]. The tunable light source is combined with a short-wave IR (SWIR) camera. The non-dispersive wavelength selection occurs already at the SC transmitter [12,24],

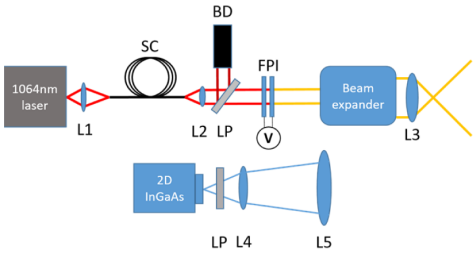


**Fig. 1.** Operating principle of the AHI. Details are explained in the text. L1-L5, convex lenses; FPI, Fabry–Perot interferometer; LP, longpass filter; BD, beam dump; SC, supercontinuum fiber.

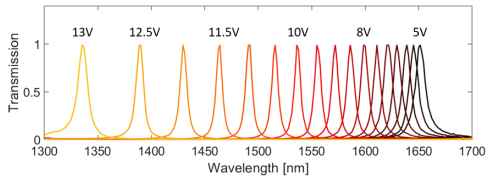


**Fig. 2.** Normalized transmission spectra of the MEMS-FPI with different operating voltages, measured at 0.5 V intervals.

as opposed to traditional HS cameras. This allows the use of any commercial imaging sensor or camera with suitable spectral sensitivity to be used for HS imaging. Filtering the wavelength channel at the transmitter also allows a simple monitoring scheme for any spectral power drifts of the SC, enabling reference target free operation. Furthermore, as only one channel is transmitted at a given time, eye safety is improved. We demonstrate an AHI capable of HS imaging in near-IR (NIR) wavelengths between 1300 nm and 1650 nm with a full width at half maximum (FWHM) less than 15 nm across the spectrum. Finally, we illustrate the potential of the imager for ice detection applications.

The operating principle of the AHI is presented in Fig. 1. SC is generated by coupling 1 ns ∼10 kW peak power pulses from a 1064 nm center wavelength microchip laser (Horus HLX-I-F020-000) with 20 kHz repetition rate into 100 m of 50 μm core graded index multimode fiber (Corning InfiniCor 50). The spectral bandwidth of the resulting SC depends on parameters such as the peak power of the pulse and type and length of the fiber. The SC generation in this work was optimized for indium gallium arsenide (InGaAs) spectral sensitivity up to 1700 nm [12].

The generated SC is first filtered with a 1300 nm longpass filter to remove any high-power residue at the pump wavelength and generated SC outside the operating range of the MEMS FPI. The filtered light is reflected into a beam dump. Light transmitted through the longpass filter goes to the MEMS FPI. Voltage applied across the FPI changes the air gap between the two opposed mirrors and tunes the resonance wavelength, as shown in Fig. 2. The MEMS FPI used in this work had a −3 dB bandwidth higher than 100 Hz. The switching time between highest and lowest wavelengths is less than 4 ms. The average power in the transmission band is approximately 200 μW per spectral channel. Light transmitted by the FPI is expanded with a beam expander [12]. A lens is used to make the beam go through a focal point and then expand to cover the field of view (FOV) of the receiver. The receiver consists of a NIR InGaAs camera (NIT WiDy SenS 640V-STP) with a 640 × 512 pixel sensor array coupled with a longpass filter and focusing optics, Thorlabs AC254-040-C and AC508-250-C for L4 and L5, respectively. The 1300 nm longpass filter is used to reduce background light outside the measurement wavelengths. A telescope consisting of two convex lenses was used to image the target plane at 3 m distance. A field programmable gate array (FPGA) based control card (National Instruments myRIO) was used to control the FPI voltage, to synchronize the wavelength selection to occur during the readout of the camera and to keep track of the wavelength channel that was used for a given frame.

The integration time for the camera was set to 180 ms. Due to acquisition delay, the total time between consequent frames was measured to be 184.4 ms, resulting in a frame rate of 5.4 Hz. A dark frame was taken before each measurement cycle and subtracted from the measurement frames. To measure the dark frame, the laser illumination was obstructed physically to avoid potential instabilities with the SC generation power-up. The measurement routine was set to record 100 frames while the MEMS FPI transmission band was scanned between 1300 nm and 1650 nm. The total acquisition time with this routine was 18.6 s for one 100-channel HS image. However, the measurement time can be reduced dramatically by selecting only the most relevant wavelength channels for each application. This is enabled by the rapidly tunable MEMS FPI. For example, three-channel false color RGB images can be acquired with frame rates higher than 1 Hz.

The spectral illumination pattern of the SC light source was studied. Any refractive components in the beam path can induce chromatic aberration, shifting the waist position for different wavelengths. This results in wavelength dependent Gaussian widths for the illumination pattern at the target plane. Even with purely reflective optics, the wavelength dependent divergence due to diffraction is enough to result in a notable difference at a few meters distance. Furthermore, there is potentially a spectral dependence of the beam quality factor (M2). In our previous work, we noticed that the SC source exhibits lower M2 for longer wavelengths, partially compensating for the larger divergence caused by diffraction [12]. In this work, the illumination pattern was calibrated by measuring a HS data cube from a diffusive plastic target, covering the whole FOV. The HS image taken from this uniform target was scaled by the maximum intensity after 2 × 2 pixel binning to produce a correction matrix for each of the 100 wavelength channels. Each channel of the following target measurements was divided by the corresponding correction matrix. An example of an illumination measurement is shown in Fig. 3. We observed some variations in both the widths and positions of the Gaussian pattern across the wavelengths. For illustration, the Gaussian fits for 1305 nm and 1650 nm are shown. Interference patterns are observed in the illumination, most likely caused by damage that was observed at the SC fiber output. The artifacts did not cause problems in this work, since the beam was profiled at the same distance as the targets were measured.

The noise performance was determined by using Allan deviation analysis. To measure the frame-to-frame noise, the wavelength channel was set to a constant value of 1600 nm, and a total of 270 frames were recorded in 50 s. The frames were averaged by 2 × 2 pixel binning to reduce noise and the effect of speckle. The Allan deviation plot for a selected pixel is shown in Fig. 4(a). The average intensity at this pixel was 314 counts. The time series of the intensity values of the pixels were divided by the mean of the time series. The Allan deviation remained

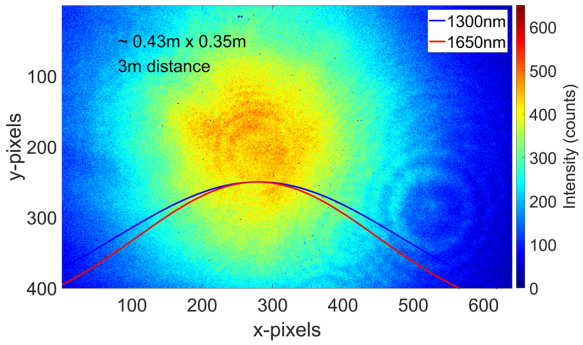


**Fig. 3.** Illumination reference measurement, measured at 3 m target distance. The intensity is shown as the mean of all wavelength channels. The target is a diffusive plastic surface. Gaussian fits for center axes are plotted for channels centered around 1305 nm and 1650 nm.

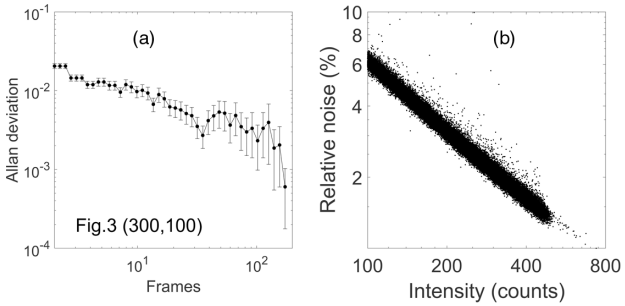


**Fig. 4.** (a) Allan deviation analysis for a time series of a selected point (300,100 for $x$, $y$ in Fig. 3) with $2 \times 2$ pixel averaging and (b) relative noise of $2 \times 2$ averaged pixels in function of signal intensity. The relative noise is plotted as $1\sigma$ standard deviation.

under 1% for at least a 25 s period, enough to measure the 100-channel HS data cube. The stability lifetime will ultimately be limited by the drifts in the SC spectrum, especially if the SC is not stabilized. In our previous work [12], we used a reference measurement integrated into the transmitter unit to correct for drifts and to damp the high pulse-to-pulse noise of the SC source. With the imaging system, pulse-to-pulse noise was not observable, because light from ∼1800 pulses was integrated in each frame. The reference measurements could enable long-term monitoring of the SC. In this work, however, the SC was turned on for 15 min before measurements, resulting in a very stable SC spectrum. The long-term stability of the SC source is characterized in [12]. The relative noise between consecutive frames in function of the signal intensity level is shown as a logarithmic plot in Fig. 4(b). The noise is plotted as $1\sigma$ standard deviation, normalized by the mean signal intensity. The systematic behavior of the noise allows for precise determination of required conditions in applications that need to have specific levels of accuracy in spectral measurement.

To demonstrate the use of the AHI for airplane icing detection, a sample was prepared using an 8 mm thick plate of 6061 aluminum, an alloy used in airplanes. Grooves of two thicknesses were machined on to the plate. The deeper groove was filled with tap water, and the plate was frozen. The thinner ice layer was created by adding water to the pre-cooled aluminum. The frozen plate was measured with the AHI within 5 min of exposure to room temperature. The aluminum plate was at a distance of 3 m from the AHI at a small angle to prevent specular

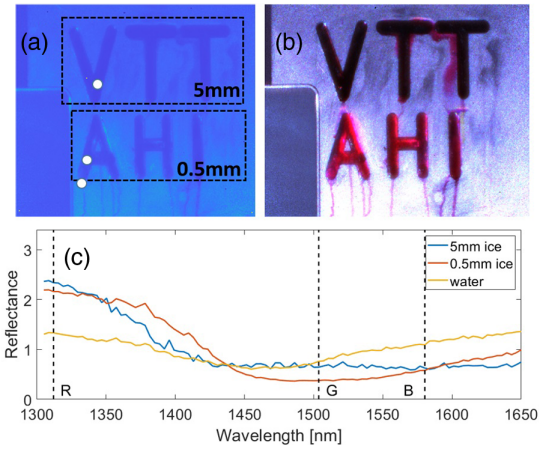


**Fig. 5.** (a) Single color image of the aluminum plate constructed by taking an average of all 100 wavelength channels. Dashed rectangles indicate the two different ice layer thicknesses of 5 mm and 0.5 mm. White circles indicate the points for the spectrum plot. (b) False color RGB representation of the HS image distinguishing the two different ice layer thicknesses and liquid water. (c) Spectra of the two ice layer thicknesses and liquid water. The dashed lines show the wavelengths selected for the false color RGB representation.

reflections. A reference target (Spectralon SRM-99) was placed next to the aluminum target plate. The measurement routine explained earlier was used to measure 100 frames, while scanning the FPI bandpass wavelength between the readout of each frame. The HS figure was constructed by first subtracting the dark frame, and then each frame was divided by the correction matrix measured prior to the target measurement to account for illumination uniformity.

A single-color image, constructed by averaging all frames (wavelengths), is shown in Fig. 5(a). The parts on the aluminum with either ice or liquid water melting from the icy parts appear darker due to lower total reflected signal. From this figure however, no conclusion can be drawn on the thickness of the ice or to separate ice and water. From the HS image, spectra representing the two different ice layers, liquid water, and the reference target were chosen from the points indicated as white spots in Fig. 5(a). The normalized reflectance spectra from these pixels are shown in Fig. 5(c). The measured intensity spectra are turned into normalized reflectance spectra by dividing the intensity spectra of the two ice layers and liquid water with the intensity spectrum from the reflectance target, shown in the left corner in the image. The reflectance values are then normalized by the mean value of the spectrum. From the spectra, clear differences can be seen between both the two ice layers and liquid water. With a deeper ice layer, more light is absorbed, and the absorption with wavelengths beyond 1450 nm start to saturate. The absorption peak moves to shorter wavelengths for liquid water as compared to ice as expected due to the phase change. Three channels were chosen for a false color RGB representation. The chosen wavelengths were centered around 1312 nm, 1504 nm, and 1580 nm for red, green, and blue, respectively. These wavelength bands have characteristics for the two ice layers and water. Furthermore, the gas phase water absorption was simulated using the HITRAN database [25] to confirm that these wavelengths are not absorbed by gas phase water. The RGB presentation of the HS image is shown in Fig. 5(b). From the RGB false color image, both ice layers can

be visually distinguished from each other, as well as the liquid water. The 5 mm and 0.5 mm ice layers are seen as dark red and red, respectively. The liquid water traces, melting from the ice layers, are seen as purple.

In conclusion, we have built and demonstrated an AHI based on the combination of a tunable MEMS FPI and SC light source. The MEMS FPI enables rapid and non-dispersive wavelength selection in the transmitter, enabling wavelength selection during the camera readout times and a simple transmission optics design. Furthermore, wavelength selection at the transmission allows simple referencing of the transmitted power, while a reference spectrometer would be required with spectrally resolving cameras. Since only the channel in use for a given frame is transmitted, eye safety is improved. The system provides flexibility to choose any imaging device with a suitable wavelength sensitivity range for HS imaging. We have shown that the system is capable of measuring HS images with reflectance spectra noise of around 1% from a 3 m distance. A measurement of an illumination reference prior to target measurement was required to account for the non-uniform illumination profile and the observed artifacts of the SC source. This may pose a limitation for applications in which the distance cannot be fixed or the target has a deep 3D structure. The instrument was demonstrated for ice detection applications, which are relevant in airplane icing monitoring or road condition monitoring. In addition, the instrument may be utilized in other areas of HS imaging such as mineral survey, food quality control, and plastic sorting. While this work focused on the 1300 nm to 1650 nm wavelength region, SC sources, MEMS FPI filters, and imaging sensors are also available in the visible region as well as in the IR region beyond the sensitivity of the InGaAs. Especially, the mid-IR (MIR) region is very attractive for many applications due to fundamental absorption bands. MIR HS imaging using passive instrumentation is particularly hindered due to the lack of illumination. The approach proposed in this work could enable practical applications that are not currently possible with the available HS imaging methods.

**Funding.** Scientific Advisory Board for Defence (MATINE); European Commission (787021); Academy of Finland (320168).

**Disclosures.** The authors declare no conflicts of interest.

**Data Availability.** Data underlying the results presented in this paper are not publicly available at this time but may be obtained from the authors upon reasonable request.

## REFERENCES

1. G. Lu and B. Fei, J. Biomed. Opt. **19**, 010901 (2014).
2. Y. Feng and D. Sun, CRC Crit. Rev. Food Sci. **52**, 1039 (2012).
3. D. Krupnik and S. Khan, Earth-Sci. Rev. **198**, 102952 (2019).
4. R. Mannila, A. Näsilä, K. Viherkanto, C. Holmlund, I. Näkki, and H. Saari, Proc. SPIE **8870**, 887002 (2013).
5. H. Saari, V. Aallos, C. Holmlund, J. Mäkynen, B. Delauré, K. Nackaerts, and B. Michiels, Proc. SPIE **7668**, 766805 (2010).
6. P. Gattinger, J. Kilgus, I. Zorin, G. Langer, R. Nikzad-Langerodi, C. Rankl, M. Gröschl, and M. Brandstetter, Opt. Express **27**, 12666 (2019).
7. Q. Yi, L. Z. Heng, L. Liang, Z. Guangcan, C. F. Siong, and Z. Guangya, Opt. Express **28**, 16126 (2020).
8. S. Yang, X. Yan, H. Qin, Q. Zeng, Y. Liang, H. Arguello, and X. Yuan, Remote Sens. **13**, 741 (2021).
9. J. M. Dudley and J. R. Taylor, *Supercontinuum Generation in Optical Fibers* (Cambridge University, 2010).
10. R. Song, J. Hou, S. Chen, W. Yang, and Q. Lu, Opt. Lett. **37**, 1529 (2012).
11. K. Yin, R. Zhu, B. Zhang, T. Jiang, S. Chen, and J. Hou, Opt. Express. **24**, 20010 (2016).
12. T. Kääriäinen, P. Jaanson, A. Vaigu, R. Mannila, and A. Manninen, Sensors **19**, 2192 (2019).
13. A. Manninen, T. Kääriäinen, T. Parviainen, S. Buchter, M. Heiliö, and T. Laurila, Opt. Express **22**, 7172 (2014).
14. T. Malkamäki, S. Kaasalainen, and J. Ilinca, Opt. Express **27**, A468 (2019).
15. A. Saleh, A. Aalto, P. Ryczkowski, G. Genty, and J. Toivonen, Opt. Lett. **44**, 4223 (2019).
16. T. Hakala, J. Suomalainen, S. Kaasalainen, and Y. Chen, Opt. Express **20**, 7119 (2012).
17. J. Kilgus, K. Duswald, G. Langer, and M. Brandstetter, Appl. Spectrosc. **72**, 634 (2018).
18. I. Zorin, R. Su, B. Heise, B. Lendl, and M. Brandstetter, J. Opt. Soc. Am. A **37**, B19 (2020).
19. M. Nischan, R. Joseph, J. Libby, and J. Kerekes, Lincoln Lab. J. **14**, 131 (2003).
20. Z. Guo, Y. Liu, X. Zheng, and K. Yin, Chin. Phys. B **28**, 034206 (2019).
21. A. Rissanen, B. Guo, H. Saari, A. Näsilä, R. Mannila, A. Akujärvi, and H. Ojanen, Proc. SPIE **10116**, 101160I (2017).
22. A. Akujärvi, B. Guo, R. Mannila, and A. Rissanen, Proc. SPIE **9760**, 97600M (2016).
23. J. Antila, A. Miranto, J. Mäkynen, M. Laamanen, A. Rissanen, M. Blomberg, H. Saari, and J. Malinen, Proc. SPIE **7680**, 76800U (2010).
24. P. Jaanson, A. Vaigu, T. Kääriäinen, R. Mannila, V. Lehtomäki, and A. Manninen, Proc. SPIE **10791**, 1079107 (2018).
25. I. E. Gordon, L. S. Rothman, C. Hill, R. V. Kochanov, Y. Tan, P. F. Bernath, M. Birk, V. Boudon, A. Campargue, K. V. Chance, and B. J. Drouin, J. Quant. Spectrosc. Radiat. Transfer **203**, 3 (2017).